Attosecond magnetization dynamics in non-magnetic materials driven by intense femtosecond lasers: supplementary information

Ofer Neufeld[1,*], Nicolas Tancogne-Dejean[1], Umberto De Giovannini[1,2], Hannes Hübener[1], and Angel Rubio[1,3,*]

[1]Max Planck Institute for the Structure and Dynamics of Matter and Center for Free-Electron Laser Science, Hamburg, Germany, 22761.
[2]Università degli Studi di Palermo, Dipartimento di Fisica e Chimica—Emilio Segrè, Palermo I-90123, Italy.
[3]Center for Computational Quantum Physics (CCQ), The Flatiron Institute, New York, NY, USA, 10010.

I. Additional results in BiH

We present here additional complimentary results to those presented in the main text. Supplementary Figure 1 presents the HHG spectra emitted from BiH in the same driving conditions as those that induce the transient magnetization discussed in the main text. Supplementary Figure 1(a) presents the HHG spectra for circularly polarized driving while tuning the laser wavelength, showing that only $6n\pm1$ harmonics (for integer n) are emitted due to dynamical symmetry considerations[1]. Supplementary Figure 1(b) presents the emitted spectra for elliptical driving, where the elliptical major axis is rotated within the monolayer plane. As seen, odd-only harmonics are emitted due to similar symmetry considerations[1]. Supplementary Figure 1(c) presents the emitted HHG spectra *vs.* the driving ellipticity (changing from circular to linear) where the main elliptical axis is along the *x*-axis (transverse to the Bi-Bi bonds). In this case we can track the harmonic emission as the system transitions from the odd-only inversion symmetry to the 6-fold rotational symmetry obtained for circularly polarized driving. The same symmetries that constrain the HHG spectral components were shown in the main text to constrain the temporal evolution of the electronic and spin excitations, clarifying that the atto-magnetic response is directly driven by the laser.

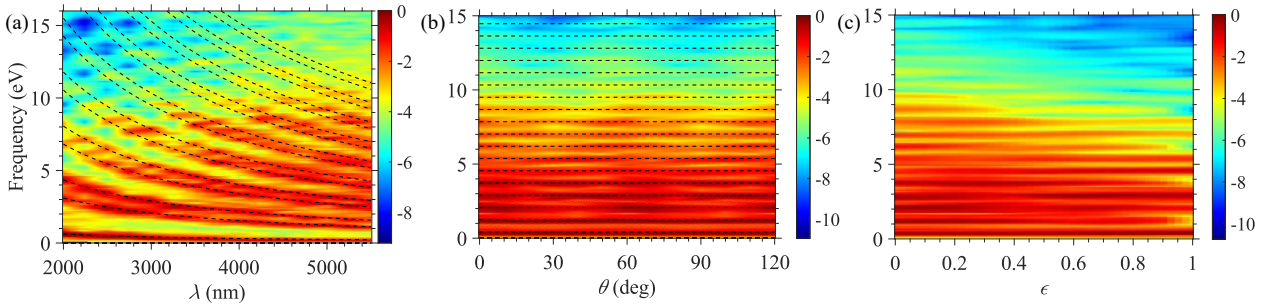

Supplementary Figure 1. HHG spectra and selection rules in BiH. (a) HHG spectra for circularly polarized driving *vs.* driving wavelength, calculated for 5×10^{12} W cm^{-2}. Dashed black lines indicate $6n\pm1$ harmonics (for integer n). (b) HHG spectra for elliptical driving with an ellipticity of 0.2, *vs.* driving angle of the elliptical major axis in the monolayer plane (for a driving wavelength of 3000nm and intensity of 2×10^{11} W cm^{-2}). Dashed black lines indicate odd harmonics. (c) HHG spectra for elliptical driving *vs.* the driving ellipticity, where the elliptical major axis is set at θ=0, for similar laser parameters as (b). All spectra are presented in log scale.

Next, we further explore the femto-magnetic response in BiH. Supplementary Figure 2(a) presents the difference in total occupations of spin-up and spin-down electrons from the ground state as the system evolves in time when driven by intense circular pulses (which is compensated for the small average ionization in both channels), Δn_α. As is clearly shown, as the system builds up a magnetic response, the occupations of spin-down states is converted to up spins, or vice versa. In fact, the occupation of spin-up states *vs.* time is formally equivalent to the calculation of $\langle S_z(t)\rangle$. Thus, this result supports the mechanism responsible for this behavior, which involves a SOC-driven flipping of spins. Supplementary Figure 2(b) presents a similar result but for circularly polarized driving with an opposite helicity, showing that there is perfect spin-helicity symmetry – exchanging light's helicity flips the magnetic response.

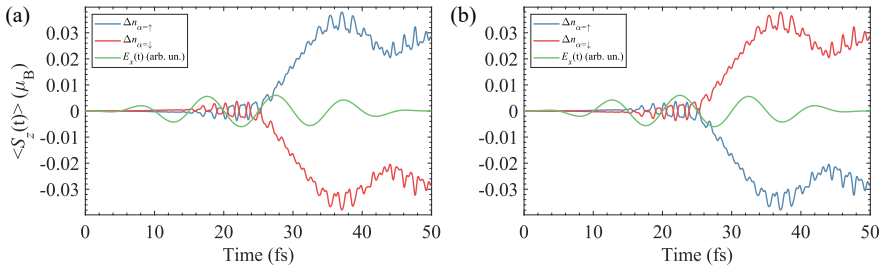

Supplementary Figure 2. Ultrafast magnetization dynamics in BiH. (a) Time-dependent occupations of spin-up and spin-down channels for circularly polarized driving (with a wavelength of 3000nm and intensity of 10^{12} W cm^{-2}). (b) same as (a) but for opposite driving light helicity. In all plots the *x*-component of the driving laser field is illustrated in arbitrary units for clarity.

We now present additional results that explore the nonlinear nature of the induced magnetism. Supplementary Figure 3(a) presents the magnetization onset time (defined as the time for which the induced magnetization temporal derivative, $\partial_t \langle S_z(t) \rangle$, surpasses $10^{-6}\,\mu_B$ per atomic unit of time) *vs.* the driving intensity for the circularly polarized driving case. The onset time behaves highly nonlinearly with the pump power, which is additional corroboration for the nonlinear nature of the effect. Supplementary Figure 3(b) presents the induced net magnetization in the same conditions as in Fig. 1(c) in the main text, with the induced total electronic excitation, n_{ex}. The plot connects the onset time of the magnetization with the light-induced excitations to the conduction band, as the two curves have a similar onset behavior. Moreover, the rapid attosecond dynamics become most prominent when the conduction band is highly populated. Similar results are obtained for other driving conditions.

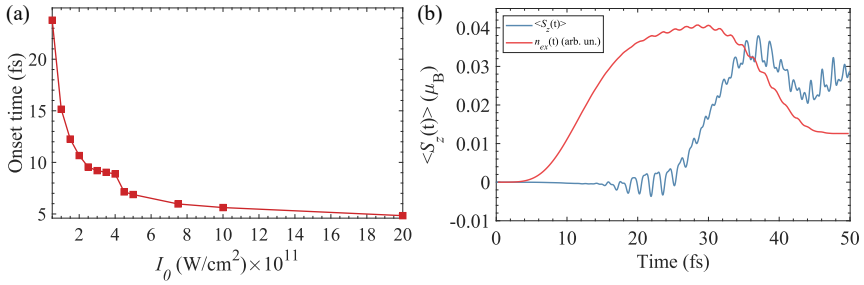

Supplementary Figure 3. Magnetization onset times and highly nonlinear nature of the magnetization dynamics in BiH. (a) Magnetization onset times *vs.* driving intensity for circularly polarized driving with a wavelength of 3000nm. (b) <S_z(t)> for circularly polarized driving with a driving wavelength of 3000nm and intensity of 5×10^{11} W cm^{-2}, and total electronic excitation in the same scale.

We next explore the connected symmetries of the electronic excitation and the spin dynamics, which further support the conclusions presented in the main text. Supplementary Figure 4(a) presents the spectral components of the electronic excitation, i.e. the Fourier transform of $n_{ex}(t)$ to the frequency-domain. This analysis allows tracking the temporal dynamics of the electronic excitation and seeing if it complies to similar symmetries as the induced magnetization. As seen in Supplementary Figure 4(a), for circularly polarized driving $n_{ex}(t)$ is comprised of only $6n$ harmonics of the driving laser (for integer n). This is a fundamental constraint that arises from dynamical symmetries[1], and complements the symmetries of the emitted HHG radiation (following $6n \pm 1$ selection rules, see Supplementary Figure 1). Essentially, Eq. (8) evaluates the sum of projections of the time-dependent wave functions onto the ground-state wave functions. However, because the dynamics of the wave functions uphold the improper-rotational dynamical symmetry in the light-matter system (which complies to $S_6 H\left(t+\frac{T}{6}\right) S_6^{\dagger} = H(t)$, where S_6 is a 6-fold improper rotation in the monolayer plane), this means that the occupations uphold $n_{ex}(t) \approx n_{ex}(t+T/6)$, where T is the laser period, which leads to the $6n$ harmonic structure. This equation is correct up to a constant shift at zero frequency that has to do with non-periodic tunneling dynamics, and symmetry breaking due to the short duration of the laser pulse (which broadens the $6n$ harmonic peaks). The inherent reason that the selection rules for $n_{ex}(t)$ are different than for the HHG emission, is that $n_{ex}(t)$ is calculated with a parity-even projection operator, whereas the dipole operator that evaluates the HHG emission is parity-odd. Nonetheless, the two selection rules have similar origins. A completely identical selection rule is obtained for the expectation value of the

total magnetization, $\langle S_z(t)\rangle$ (e.g. as seen in Fig. 2 in the main text, and in Supplementary Figure 4(b)), also allowing only $6n$ harmonics. It means that the two quantities of $n_{ex}(t)$ and $\langle S_z(t)\rangle$ are inherently connected, because the induced magnetization is physically driven by the excitations to the conduction band.

Supplementary Figure 4(c) further presents the spectral components of $n_{ex}(t)$ for a system driven by an elliptically-polarized pulse. In this case, the light-matter system follows a dynamical inversion symmetry ($\mathrm{i}H\left(t+\frac{T}{2}\right)\mathrm{i}^{\dagger}=H(t)$, where i is an inversion operator), which means that the projections follow $n_{ex}(t) \approx n_{ex}(t+T/2)$, leading to even-only harmonics. This complements the odd-only HHG emission (see Supplementary Figure 1) and has an identical origin. Supplementary Figure 4(d) presents the spectral components of $\langle S_z(t)\rangle$ for the same conditions, also showing even-only harmonics further supporting the generality of the mechanism presented in the main text. We obtained similar results that connect the symmetries of the light-driven currents, the electronic excitation, and the induced magnetization, in all explored conditions.

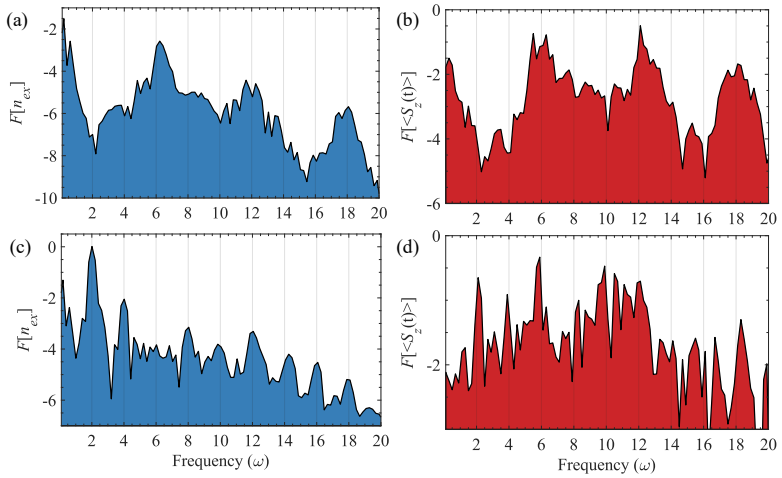

Supplementary Figure 4. Symmetries of the electronic excitation and their connection to magnetization dynamics in BiH. (a) Spectral components for n_{ex}(t) plotted in arbitrary units in log scale for circularly polarized driving (with wavelength of 3000nm and intensity of 5×10^{11} W cm^{-2}). The *x*-axis is given in units of the laser frequency, and even harmonics are indicated with grey lines. Only 6*n* harmonics are observed with circularly polarized driving (for integer *n*). (b) Same as (a) but for <S_z(t)> in similar conditions, showing similar symmetry-based selection rules. (c) Same as (a) but for elliptical driving with an ellipticity of 0.5, a major elliptical axis angle of θ=30^0, and driving intensity of 2×10^{11} W cm^{-2}. Only even harmonics of the drive are observed. Same as (c), but for <S_z(t)> in similar conditions, showing similar symmetry-based selection rules.

We now present the band- and *k*-space-resolved induced magnetization. The band-resolved contributions to the magnetization were calculated by projecting the time-dependent wave functions onto the ground-state wave functions, just as was done for $n_{ex}(t)$. However, in this case the projections were not summed in *k*-space and over the bands, and instead, the *k*-resolved projections for pairs of spin-degenerate bands were summed together after weighting the occupations by the expectation value $\langle S_z\rangle$ at that particular band and *k*-point. This gives a measure for the different contributions of each band and *k*-point to the induced magnetization, and for instance at *t=0* this analysis leads to identically zero magnetization in all bands and *k*-points (because the initial state is non-magnetic). Figures S5(a-d) presents these results for a circularly polarized driving case after the laser pulse ends for the first and second valence and conduction bands (in the notation where the 'first' bands includes two spin-degenerate bands, and so on). As is seen, the dominant contribution to the magnetization arises from regions near the minimal band gap (K and K' points). Moreover, the first valence and conduction band contribute stronger magnetic responses than other bands. This trend continues in higher bands (not presented). These results thus support that the first step in the mechanism behind the induced magnetization is electronic excitation to the conduction band, as discussed in the main text. In contrast to these results, Figs. S5(e,f) present the complementary *k*- and band-resolved magnetization after the interaction with a linear driving pulse for the first valence and conduction bands. Here, each region around K and K' contributes to both positive and negative magnetization, and the magnetization at K and K' is inverted, such that the net magnetism overages out to zero, as expected for linear driving.

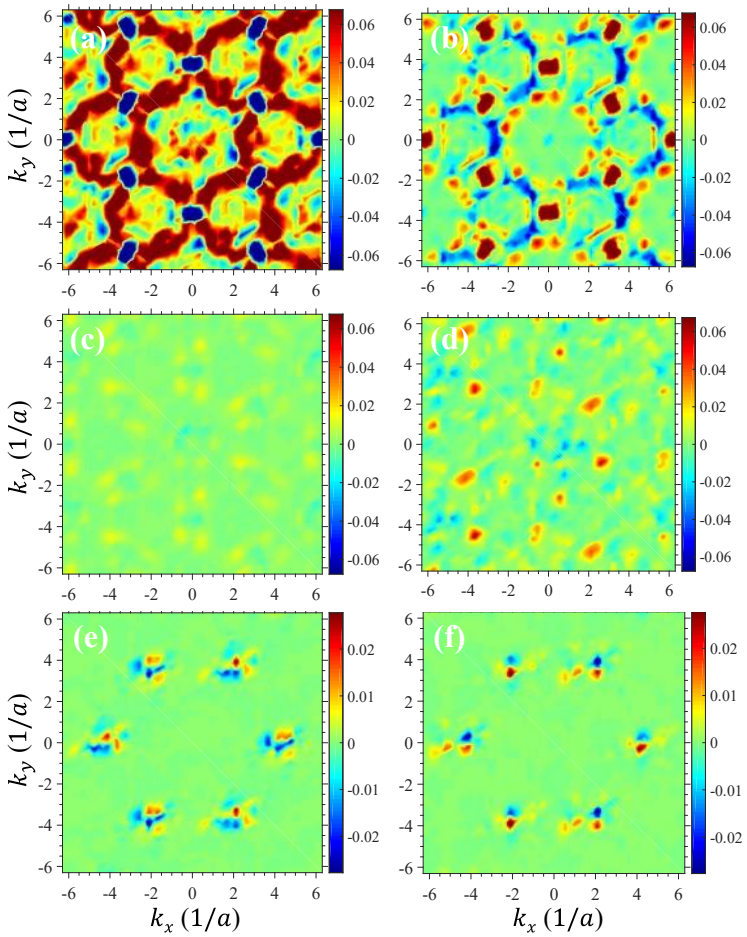

Supplementary Figure 5. *k*- and band-resolved projections of the light-induced net magnetization after the pulse. (a-d) Magnetization after circularly polarized driving with a wavelength of 3000nm and intensity of 7.5×10^{11} W cm^{-2}. (a) First valence band, (b) first conduction band, (c) second valence band, (d) second conduction band. (e,f) Same as (a,b), respectively, but for linear driving with an intensity of 2×10^{11} W cm^{-2} and a polarization axis at $\theta=20^0$.

We also tested the role of correlations in the ultrafast induced magnetization dynamics. We have thus far employed TDSDFT in the local spin density approximation for the XC functional, which allows the *e-e* interactions to evolve dynamically in time. However, it is helpful to explore the role of correlations by employing the independent particle approximation (IPA), which is equivalent to freezing the time-evolution of the XC potential, and the time-evolution of the Hartree term. Within this approach the time propagation of all the KS-Bloch states is fully independent of each other, and dynamical *e-e* interactions are not included in the simulation. Supplementary Figure 6(a) presents the spin expectation value in circularly polarized driving, comparing the IPA to the full TDSDFT calculation. As is clearly seen, the magnetization dynamics are not driven by correlations as a very similar response is obtained within the IPA.

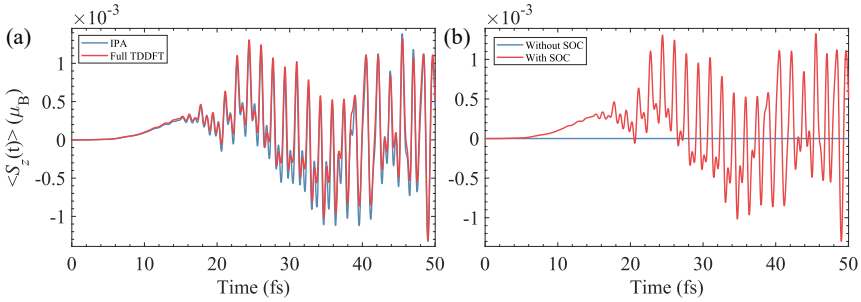

Supplementary Figure 6. Comparison of different levels of theory on the induced magnetic response. (a) <S_z(t)> in BiH calculated with full TDSDFT compared to IPA for circularly polarized driving, with a wavelength of 3000nm and a intensity of 2×10^{11} W cm^{-2}. (b) Same as (a) but comparing the TDSDFT calculation with and without SOC term.

Next, we explicitly verified the integral role of SOC in the spin-flipping mechanism. This was accomplished by performing a TDSDFT calculation within the LDA, but while turning on/off the SOC term. Supplementary Figure 6(b) presents the induced magnetic response driven by a circularly-polarized laser field for both cases (where in the calculation without SOC only up/down channels were incorporated rather than full non-collinear spins). The results clearly show that the induced magnetization identically vanishes in the absence of SOC, while it is nonzero with SOC. Fundamentally, this arises since the SOC term is the only non-diagonal term in spin-space in the KS equations of motion, such that only it allows coupling the different spin channels (as further discussed in the main text).

II. Additional results in $MoTe_2$

We present here additional complimentary results to those presented in the main text for the $MoTe_2$ material system, both in monolayer and bulk phases. For the monolayer, Supplementary Figure 7(a) presents the spin expectation value driven by a circular pump, showing a femtosecond turn-on of magnetism that is in correspondence with the results obtained in the main text. The electronic excitation matches in onset time with the onset of magnetization (see Supplementary Figure 7(a)). Supplementary Figure 7(b) presents the spectral components of $n_{ex}(t)$ in the same driving conditions, showing that in this case only $3n$ components (for integer n) are allowed (because a monolayer of H-$MoTe_2$ is 3-fold symmetric instead of 6-fold). Similarly, Supplementary Figure 7(c) presents the spectral components of $\langle S_z(t)\rangle$ that also support only $3n$ harmonics. These results arise from the different symmetries of $MoTe_2$ compared to BiH. It demonstrates the generality of our analysis.

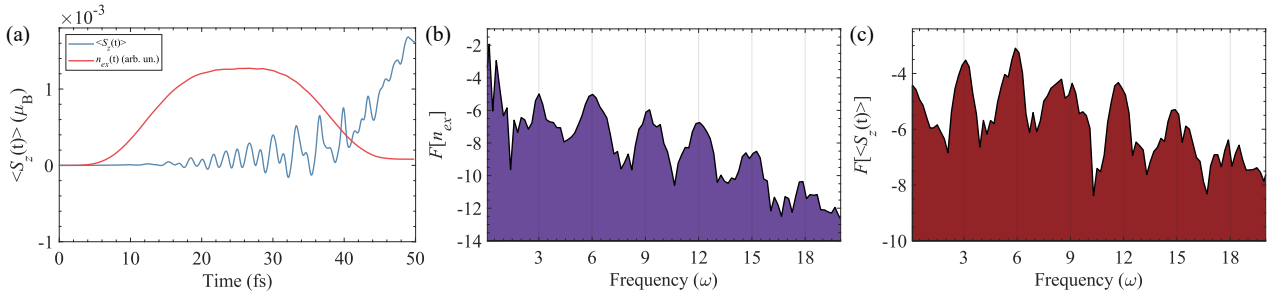

Supplementary Figure 7. Additional results for light-induced magnetization dynamics in monolayer H-$MoTe_2$. (a) <S_z(t)> and n_{ex}(t) for circularly polarized driving with a wavelength of 3000nm and intensity of 2×10^{11} W cm^{-2}. (b) Spectral components of n_{ex}(t) plotted in log scale for the same driving conditions as in (a). The *x*-axis is given in units of the laser frequency, and every 3rd harmonic is indicated with grey lines. Only 3*n* harmonics are observed with circularly polarized driving (for integer *n*). (c) Same as (b) but for <S_z(t)> in similar conditions, showing similar symmetry-based selection rules. (b) and (c) are plotted in arbitrary units in log scale.

Supplementary Figure 8 presents results for the 2H bulk phase of $MoTe_2$ for circular and linear driving. For the circular case (Supplementary Figure 8(a,b)) we obtain a femtosecond turn-on of the magnetic response which is comprised of $6n$ harmonics of the pump laser, owing to the inherent symmetries of the bulk 2H phase driven by circular light (the bulk phase exhibits a 6-fold rotation coupled to a glide symmetry along the *c*-axis). For the linear case we obtain attosecond magnetization dynamics, in similar spirit to the results in the main text, which comprise of even-only harmonics of the laser (see Supplementary Figure 8(c,d)). Thus, the results in the bulk phase support the results obtained in the monolayer systems, and demonstrate that the effect is valid in 3D bulk systems.

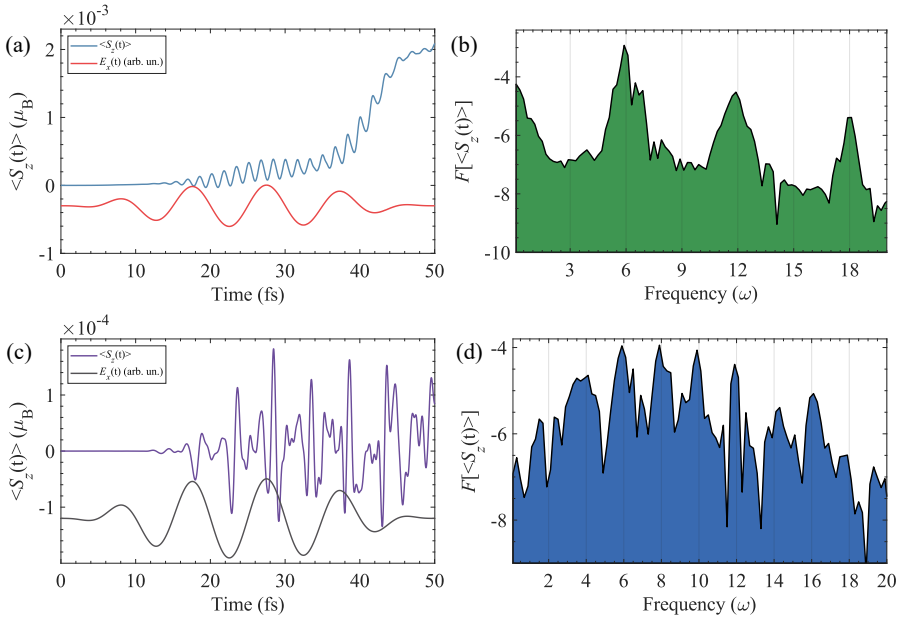

Supplementary Figure 8. Femtosecond turn-on of magnetization and attosecond magnetization dynamics in bulk 3D 2H-MoTe2. (a) $<S_z(t)>$ for circularly polarized driving with a wavelength of 3000nm and intensity of 2×10^{11} W cm^{-2}. The *x*-component of the driving field is illustrated in arbitrary units to convey the different timescales in the dynamics. (b) Spectral components of $<S_z(t)>$ plotted in log scale for the same driving conditions as in (a). The *x*-axis is given in units of the laser frequency, and every 3rd harmonic is indicated with grey lines. Only 6*n* harmonics are observed with circularly polarized driving (for integer *n*). (c) Same as (a) but for linearly polarized driving with $\theta=10^0$. (d) same as in (b) but for the driving conditions in (c). Every 2nd harmonic is illustrated by grey lines, and only even harmonics are observed. (b) and (d) are plotted in arbitrary units in log scale.

III. Additional results in Na_3Bi

We present additional complimentary results to those presented in the main text for Na_3Bi, the Dirac semimetal. Supplementary Figure 9 shows the induced magnetization dynamics driven by intense linearly-polarized light in the hexagonal planes for two different driving angles (either along a high-symmetry axis, or not). As clearly shown, when Na_3Bi is not driven along high symmetry axis it permits a strong oscillating magnetization. We verified that this is a result of nonzero transverse currents that permit transient orbital angular momentum (not presented). On the other hand, along high symmetry axes the transverse currents are not permitted, leading to an identically vanishing magnetism. Thus, these results support the generality of our conclusions, even in materials with vanishing Berry curvature.

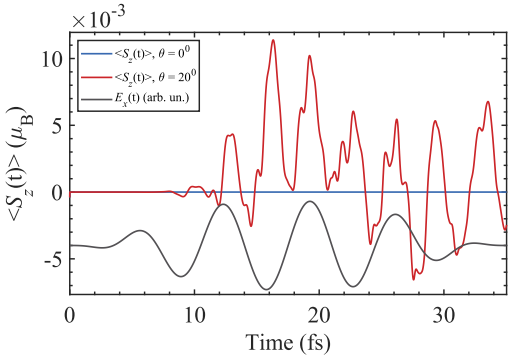

Supplementary Figure 9. Attosecond magnetization dynamics in the Dirac semimetal Na_3Bi for linearly polarized driving with a wavelength of 2100nm and intensity of 7×10^{11} W cm^{-2}. The *x*-component of the driving field is illustrated in arbitrary units to convey the different timescales in the dynamics. The plots show the magnetic response for driving in the *xy* plane either along a mirror axis ($\theta=0$), or at an angle of 20^0 from that axis.

Supplementary References

1. Neufeld, O., Podolsky, D. & Cohen, O. Floquet group theory and its application to selection rules in harmonic generation. *Nat. Commun.* **10**, 405 (2019).